

Coherent-incoherent crossover of the intrinsic spin Hall effect in PdSatoshi Haku,¹ Hiroyuki Moriya,¹ Hongyu An,² Akira Musha,¹ and Kazuya Ando^{1,3,4,*}¹*Department of Applied Physics and Physico-Informatics, Keio University, Yokohama 223-8522, Japan*²*College of New Materials and New Energies, Shenzhen Technology University, Shenzhen 518118, People's Republic of China*³*Keio Institute of Pure and Applied Sciences, Keio University, Yokohama 223-8522, Japan*⁴*Center for Spintronics Research Network, Keio University, Yokohama 223-8522, Japan* (Received 11 July 2021; revised 31 August 2021; accepted 19 October 2021; published 2 November 2021)

We report the coherent-incoherent crossover of the spin Hall effect in Pd. By measuring spin-orbit torques generated by oxygen-incorporated Pd films, we find two distinct regimes of the spin Hall effect; one in which the spin Hall conductivity is insensitive to the electric conductivity, and the other in which the spin Hall conductivity decreases with decreasing electric conductivity. The crossover between the two regimes is consistent with the prediction of the coherent-incoherent crossover of the spin Hall effect, which is analogous to that of the anomalous Hall effect. Unlike the anomalous Hall effect, for which the crossover has been observed for a wide class of ferromagnets, the crossover of the spin Hall effect has been confirmed only for Pt and Pt-based alloys. The observation of the crossover of the spin Hall effect for Pd supports the generality of this phenomenon, illustrating an important correspondence between the spin Hall effect and the anomalous Hall effect.

DOI: [10.1103/PhysRevB.104.174403](https://doi.org/10.1103/PhysRevB.104.174403)**I. INTRODUCTION**

Spin-orbit coupling is responsible for a variety of phenomena in magnetism and spintronics [1]. One of intriguing phenomena arising from the spin-orbit coupling is the spin Hall effect, which was theoretically predicted about half a century ago [2]. The spin Hall effect converts a charge current into a spin current and vice versa, enabling electric generation and detection of spin currents [3–10]. This effect has been central in the recent discoveries of spin-orbit coupling phenomena in spintronics [11].

The spin Hall effect originates from the extrinsic scattering or the intrinsic Berry curvature mechanisms [11–14]. The extrinsic contribution to the spin Hall effect is dominant only in superclean systems because this contribution is strongly diminished by carrier scattering. In most heavy metals, the spin Hall effect is dominated by the intrinsic mechanism, which is robust against carrier scattering when the scattering time is sufficiently long [11]. In this regime, the intrinsic spin Hall conductivity is governed by interband excitations between spin-orbit split bands [15], and the intrinsic spin Hall conductivity is insensitive to carrier scattering. By further decreasing the carrier scattering time, the system enters the incoherent regime. In this regime, the spin Hall conductivity decreases with decreasing scattering time because the scattering limits the interband excitation that governs the intrinsic spin Hall effect [16]. The crossover between the coherent and incoherent regimes has been observed for the anomalous Hall effect, which shares the same mechanism as the spin Hall effect [17]. The observation of the crossover of the anomalous Hall effect for a wide class of ferromagnets demonstrates the generality of this phenomenon, providing important information for the fundamental understanding of spin-transport physics.

The crossover of the spin Hall effect has recently been demonstrated experimentally [18–22]. This finding illustrates an important correspondence between the spin and anomalous Hall effects. However, unlike the anomalous Hall effect, which has been investigated for a wide class of ferromagnets [23–25], the crossover of the spin Hall effect has been confirmed only for Pt and Pt-based alloys. Despite the theoretical prediction that the coherent-incoherent crossover of the spin Hall effect is ubiquitous in many transition metals [16], experimental evidence of the generality of the crossover is still lacking.

In this work, we demonstrate the coherent-incoherent crossover of the spin Hall effect in Pd. We investigate the spin Hall effect in Pd by measuring the spin-torque ferromagnetic resonance (ST-FMR) for Ni₈₁Fe₁₉/Pd films, where the electric conductivity of Pd films is varied by incorporating oxygen. Recently, it has been shown that oxygen incorporation offers an effective way to manipulate the effective spin Hall conductivity of metals [26–32]. We find a rapid decay of the spin Hall conductivity with decreasing conductivity for oxygen-incorporated Pd films, where the oxygen atoms are primarily dispersed in the Pd layer as intersite impurities. The suppression of the spin Hall conductivity is consistent with the prediction of the spin Hall effect in the dirty regime where the carrier scattering limits the interband excitation that governs the intrinsic spin Hall effect. This result demonstrates the generality of the coherent-incoherent crossover of the spin Hall effect.

II. EXPERIMENTAL DETAILS**A. Sample characteristics**

The devices used for the ST-FMR measurements are thin films consisting of a 1-nm-thick TiO₂ layer, followed by a 10-nm-thick oxygen-incorporated Pd, Pd(O), layer, and a

*ando@appi.keio.ac.jp

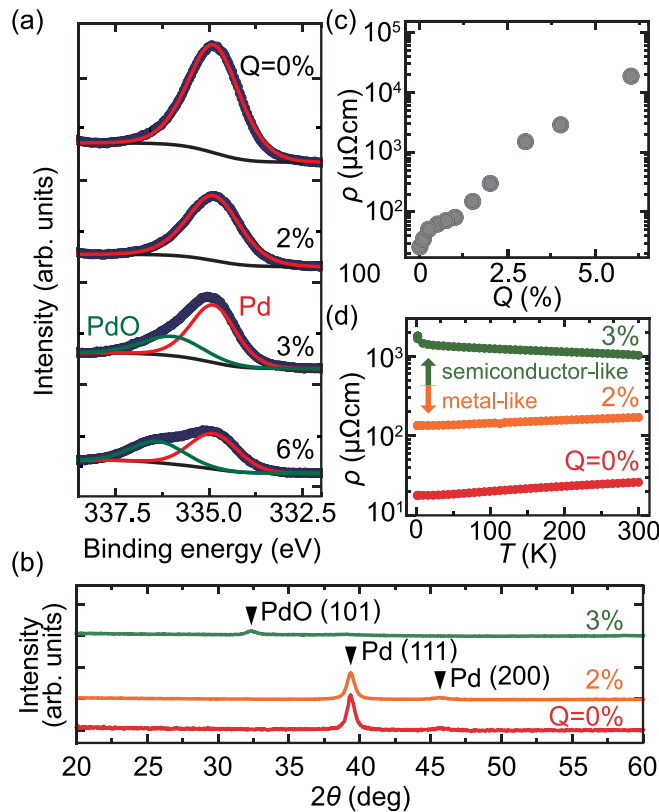


FIG. 1. (a) The Pd $3d_{5/2}$ XPS spectra for the Pd film with $Q = 0\%$ and Pd(O) films with $Q = 2\%$, 3% , and 6% . The binding energy of $3d_{5/2}$ is 335.3 ± 0.2 eV for Pd and 336.3 ± 0.2 eV for PdO [33]. (b) The XRD patterns from the Pd film with $Q = 0\%$ and Pd(O) films with $Q = 2\%$ and 3% . (c) Q dependence of the electric resistivity ρ of the Pd(O) films. (d) The temperature T dependence of the electric resistivity ρ of the Pd film with $Q = 0\%$ and Pd(O) films with $Q = 2\%$ and 3% . For the resistivity measurements, 10-nm-thick Pd(O) films were patterned into Hall bars with a width of $20 \mu\text{m}$ and a length of $80 \mu\text{m}$. The resistance was measured by the conventional four-probe method.

8-nm-thick $\text{Ni}_{81}\text{Fe}_{19}$ layer, capped with a 3-nm-thick SiO_2 layer. The films, except for the deposition of the Pd(O) layer, were grown on thermally oxidized SiO_2 substrates by radio frequency (rf) magnetron sputtering by applying argon gas with a flow rate of 10 standard cubic centimeters per minute (sccm). The Pd(O) layer was sputtered in the mixture of argon and oxygen gas. The ratio Q of the oxygen gas flow rate to the total gas flow rate was varied from 0% to 3%, where the total gas flow rate was fixed at 10 sccm. The base pressure in the chamber before the deposition was better than 1×10^5 Pa and the deposition pressure was 0.24 Pa. The thicknesses of each layer were controlled by the deposition time with precalibrated deposition rates.

For the Pd(O) films, the chemical profile was investigated using x-ray photoelectron spectroscopy (XPS) with Mg $K\alpha$ radiation (1253.6 eV) and a hemispherical energy analyzer (transit energy: 10 eV, resolution: 0.03 eV). Figure 1(a) shows the Pd $3d_{5/2}$ XPS spectra for the Pd films fabricated with different Q . This result shows that only the Pd peak is observed for the Pd film with $Q = 0\%$ and Pd(O) film with $Q = 2\%$.

By further increasing Q , the PdO peak appears in addition to the Pd peak. This result also shows that the ratio of PdO to Pd increases with increasing Q .

To investigate the microstructure of the Pd(O) films, the x-ray diffraction (XRD) was measured using Cu $K\alpha$ ($\lambda = 1.5405 \text{ \AA}$) radiation by changing the irradiation angle from 10° to 70° in 0.01° steps, as shown in Fig. 1(b). For the Pd film with $Q = 0\%$ and Pd(O) film with $Q = 2\%$, we find the XRD peaks at around 39.3° and 46.7° . These peaks are attributed to Pd(111) and Pd(200), respectively [34], indicating that the crystallinity of the Pd film is unchanged by the oxygen incorporation for $Q \leq 2\%$. These XRD peaks disappear by increasing Q ; for the Pd(O) film with $Q = 3\%$, we find the XRD peak at around 33.9° , which corresponds to PdO(101) [35,36].

The XPS and XRD results suggest that, for $Q \leq 2\%$, the oxygen atoms are primarily dispersed in the Pd film as intersite impurities rather than being substituted into the Pd lattice. The formation of PdO is non-negligible only for $Q > 2\%$. To confirm this, we also measured Q and temperature T dependence of the electric resistivity ρ of the Pd(O) films. In Fig. 1(c), we show the Q dependence of ρ . This result shows that ρ increases with increasing Q , supporting that the oxygen concentration in the Pd film is controlled by Q . In Fig. 1(d), we show the T dependence of ρ . This result shows that, for the Pd film with $Q = 0\%$ and the Pd(O) film with $Q = 2\%$, ρ decreases with decreasing T . This metallic behavior of the resistivity supports the idea that the oxygen atoms are primarily dispersed in the Pd as intersite impurities, and the essential band structure of Pd is maintained. The T dependence of ρ changes by increasing Q from 2% to 3%; ρ increases with decreasing T for the Pd(O) film with $Q = 3\%$, as shown in Fig. 1(d). This semiconductor-like behavior of the resistivity is consistent with the formation of PdO for $Q = 3\%$. For the ST-FMR study, we focus on the Pd and Pd(O) films with $Q \leq 2\%$, where the oxygen atoms are primarily dispersed in the Pd film as intersite impurities, and the essential band structure of Pd is maintained.

B. Spin-torque ferromagnetic resonance

For the ST-FMR measurement, the $\text{Ni}_{81}\text{Fe}_{19}/\text{Pd(O)}$ films were patterned into $100 \mu\text{m} \times 10 \mu\text{m}$ stripes using the photolithography and liftoff techniques. Figure 2(a) shows a schematic illustration of the ST-FMR device, where a rf current was applied along the longitudinal direction of the device, and an in-plane magnetic field H was applied at an angle of 45° from the longitudinal direction. In the device, the resistivity of the Pd(O) films with $Q \leq 2\%$ is comparable to that of $\text{Ni}_{81}\text{Fe}_{19}$, $106 \mu\Omega\text{cm}$ [see also Fig. 1(c)]. The rf current flowing in the Pd(O) layer generates spin-orbit torques, including the damping-like (DL) torque and the field-like (FL) torque. These torques, as well as the Oersted field, drive the precession of the magnetization in the $\text{Ni}_{81}\text{Fe}_{19}$ layer. The precessing magnetization results in an oscillation of the device resistance due to the anisotropic magnetoresistance (AMR). We measured a direct current (dc) voltage V_{mix} arising from the mixing of the rf charge current and oscillating resistance using a bias tee at room temperature.

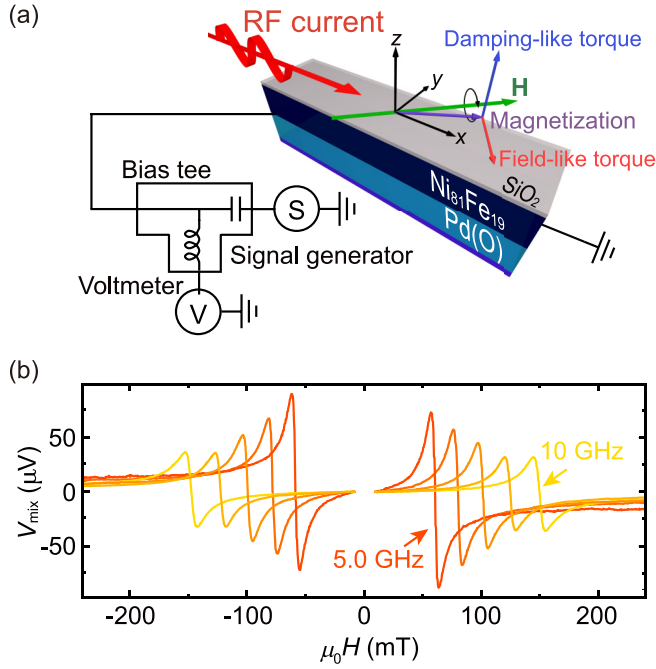


FIG. 2. (a) Schematic of the $\text{SiO}_2(2 \text{ nm})/\text{Ni}_{81}\text{Fe}_{19}(8 \text{ nm})/\text{Pd}(\text{O})(10 \text{ nm})/\text{Ti}(1 \text{ nm})$ device structure. (b) The ST-FMR spectra V_{mix} for the $\text{Ni}_{81}\text{Fe}_{19}/\text{Pd}$ film with $Q = 0\%$ at the frequency from 5.0 to 10 GHz. The applied microwave power is 24.7 dBm.

III. RESULTS AND DISCUSSION

Figure 2(b) shows the V_{mix} spectra for the $\text{Ni}_{81}\text{Fe}_{19}/\text{Pd}$ film with $Q = 0\%$ at frequencies f varied from 5.0 to 10 GHz. This result shows that the V_{mix} signal changes with f , consistent with the prediction of the voltage generation induced by the ST-FMR. Here, the ST-FMR signal V_{mix} is expressed as [37]

$$V_{\text{mix}} = V_S \frac{W^2}{(\mu_0 H - \mu_0 H_R)^2 + W^2} + V_A \frac{W(\mu_0 H - \mu_0 H_R)}{(\mu_0 H - \mu_0 H_R)^2 + W^2}, \quad (1)$$

where V_S and V_A are the magnitudes of the symmetric and antisymmetric components, respectively. W is the linewidth, and H_R is the FMR field.

In Figs. 3(a) and 3(b), we show fitting results for the V_{mix} spectra using Eq. (1) for the $\text{Ni}_{81}\text{Fe}_{19}/\text{Pd}$ film with $Q = 0\%$ and $\text{Ni}_{81}\text{Fe}_{19}/\text{Pd}(\text{O})$ film with $Q = 2.0\%$. The fitting results in Figs. 3(a) and 3(b) show that the symmetric component V_S is almost unchanged, while the antisymmetric component V_A is clearly suppressed by the oxygen incorporation. To characterize the change in V_S and V_A , we calculate the FMR spin-orbit torque efficiency [37],

$$\xi_{\text{FMR}} = \frac{V_S}{V_A} \frac{e}{\hbar} \mu_0 M_s t_{\text{FM}} d_{\text{NM}} \sqrt{1 + \frac{M_{\text{eff}}}{H_R}}, \quad (2)$$

where e is the elementary charge and \hbar is the reduced Planck constant. t_{FM} and d_{NM} represent the thicknesses of the $\text{Ni}_{81}\text{Fe}_{19}$ and $\text{Pd}(\text{O})$ layers, respectively. The saturation magnetization M_s and the effective demagnetization field $4\pi M_{\text{eff}}$ can be determined from the relation between f

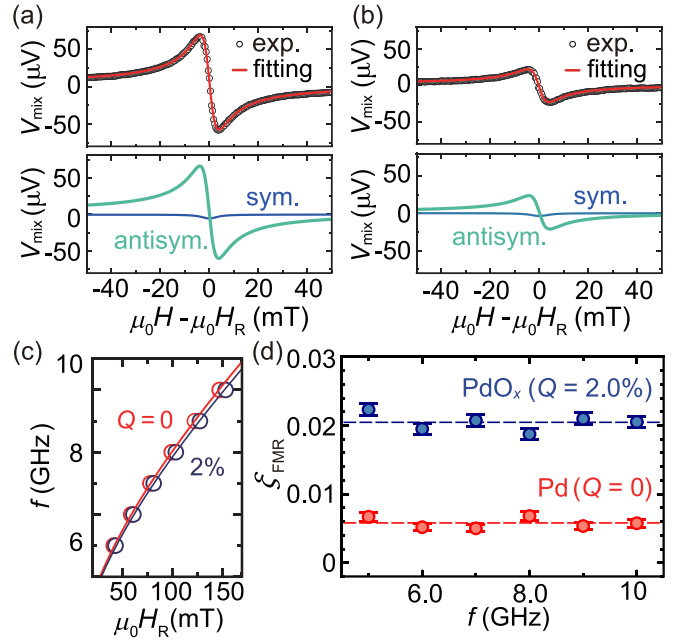


FIG. 3. The ST-FMR spectrum for the (a) Pd film with $Q = 0\%$ and (b) Pd(O) film with $Q = 2\%$ at 7 GHz. The symmetric and antisymmetric components of the fitting results are plotted correspondingly. (c) The relation between the frequency f of the applied current and the FMR field H_R . The open circles in red ($Q = 0\%$) and black ($Q = 2\%$) are the experimental data. The solid curves are the fitting result using the Kittel formula. (d) The f dependence of the FMR spin-orbit torque efficiency ξ_{FMR} for the $\text{Ni}_{81}\text{Fe}_{19}/\text{Pd}$ film with $Q = 0\%$ and $\text{Ni}_{81}\text{Fe}_{19}/\text{Pd}(\text{O})$ film with $Q = 2.0\%$.

and H_R , shown in Fig. 3(c), using the Kittel formula $f = \frac{\gamma}{2\pi} \sqrt{\mu_0 H_R (\mu_0 H_R + \mu_0 M_{\text{eff}})}$, where γ is the gyromagnetic ratio. Using the extracted parameters, we plot the f dependence of ξ_{FMR} in Fig. 3(d). This result demonstrates that ξ_{FMR} is independent of f , which supports that the observed V_{mix} signals are dominated by the ST-FMR; the inverse spin Hall voltage induced by spin pumping and thermoelectric effects are negligible in the measured signals [38,39]. We also note that ξ_{FMR} is enhanced by the oxygen incorporation; the average value of ξ_{FMR} is $\xi_{\text{FMR}} = 0.0058 \pm 0.0007$ for the $\text{Ni}_{81}\text{Fe}_{19}/\text{Pd}$ film with $Q = 0\%$ and $\xi_{\text{FMR}} = 0.0204 \pm 0.0011$ for the $\text{Ni}_{81}\text{Fe}_{19}/\text{Pd}(\text{O})$ film with $Q = 2\%$. Here, ξ_{FMR} corresponds to the effective spin Hall angle when the FL torque is negligible [40], suggesting that the effective spin Hall angle is enhanced by the oxygen incorporation. However, the FL torque has been suggested to be non-negligible in ferromagnetic-metal/Pd films [41], and thus it is necessary to disentangle the Oersted field and FL effective field in the $\text{Ni}_{81}\text{Fe}_{19}/\text{Pd}$ and $\text{Ni}_{81}\text{Fe}_{19}/\text{Pd}(\text{O})$ films, as discussed below.

We determine the DL effective field H_{DL} and the FL effective field H_{FL} for the $\text{Ni}_{81}\text{Fe}_{19}/\text{Pd}$ and $\text{Ni}_{81}\text{Fe}_{19}/\text{Pd}(\text{O})$ films. In the ST-FMR spectra, the symmetric component V_S is proportional to H_{DL} as [42]

$$V_S = \frac{I_{\text{rf}} \Delta R}{2} A_{\text{sym}} \mu_0 H_{\text{DL}} \sin \theta, \quad (3)$$

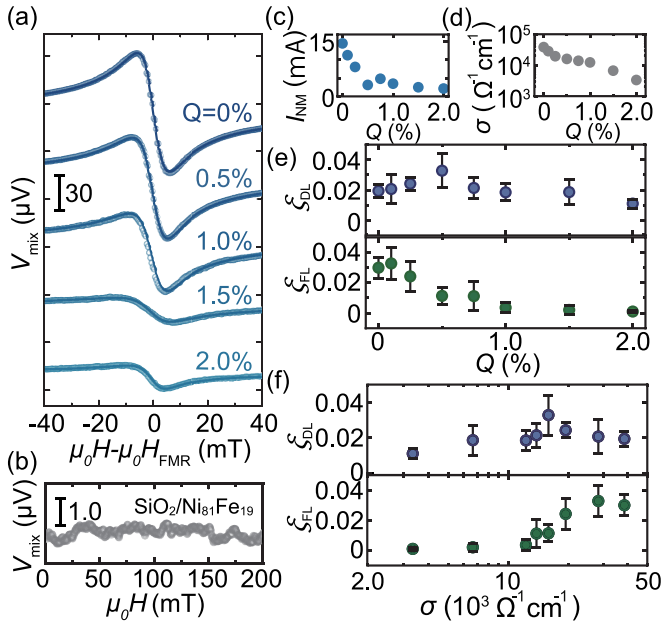


FIG. 4. (a) The ST-FMR spectra for the $\text{Ni}_{81}\text{Fe}_{19}/\text{Pd}(\text{O})$ films with different Q at 7 GHz. The open circles are the experimental data, and the solid curves are the fitting result using Eq. (1). (b) The ST-FMR spectrum for the $\text{SiO}_2/\text{Ni}_{81}\text{Fe}_{19}/\text{SiO}_2$ -substrate device at 7 GHz. (c) The Q dependence of the rf current in the Pd(O) layer, I_{NM} . (d) The Q dependence of the electric conductivity σ of the Pd(O) films. (e) The Q dependence of the DL and FL torque efficiency, ξ_{DL} and ξ_{FL} , for the $\text{Ni}_{81}\text{Fe}_{19}/\text{Pd}(\text{O})$ film. (f) The Pd(O)-layer conductivity σ dependence of ξ_{DL} and ξ_{FL} for the $\text{Ni}_{81}\text{Fe}_{19}/\text{Pd}(\text{O})$ film.

while the antisymmetric component V_A is proportional to the sum of H_{FL} and the Oersted field h_{Oe} as

$$V_A = \frac{I_{\text{rf}} \Delta R}{2} A_{\text{antisym}} (\mu_0 H_{\text{FL}} + \mu_0 h_{\text{Oe}}) \cos \theta, \quad (4)$$

where ΔR and θ are the AMR amplitude of the device and the angle between the magnetization and the flow direction of the rf current, respectively. $I_{\text{rf}} = I_{\text{FM}} + I_{\text{NM}}$ is the rf current flowing in the device, where I_{FM} and I_{NM} are the rf current in the $\text{Ni}_{81}\text{Fe}_{19}$ and Pd(O) layers, respectively. A_{sym} and A_{antisym} are coefficients described as $A_{\text{sym}} = \gamma(H_{\text{R}} + M_{\text{eff}})H_{\text{R}}/[\omega W(2H_{\text{R}} + M_{\text{eff}})]$ and $A_{\text{antisym}} = (H_{\text{R}} + M_{\text{eff}})/[W(2H_{\text{R}} + M_{\text{eff}})]$, where $\omega = 2\pi f$. We determined I_{rf} by monitoring the resistance change due to the Joule heating [42], and ΔR by assuming a parallel resistor model. The Oersted field h_{Oe} can be estimated using $\mu_0 h_{\text{Oe}} = \mu_0 I_{\text{NM}}/2(w + d)$. w and d are the width and thickness of the Pd(O) layer, respectively. In Fig. 4(a), we show typical ST-FMR signals for the devices with different Q . We have also confirmed that the ST-FMR signal is negligible in a $\text{SiO}_2/\text{Ni}_{81}\text{Fe}_{19}$ film, fabricated on a SiO_2 substrate, as shown in Fig. 4(b). This result supports the idea that the V_{mix} signals observed for the $\text{Ni}_{81}\text{Fe}_{19}/\text{Pd}(\text{O})$ films are dominated by the current-induced torques originating from the Pd(O) layer. Using the measured values of V_S and V_A with Eqs. (3) and (4), we obtain the DL(FL) torque efficiencies [40],

$$\xi_{\text{DL(FL)}} = \frac{2e}{\hbar} \mu_0 M_s t_{\text{FM}} \frac{H_{\text{DL(FL)}}}{j_{\text{NM}}}, \quad (5)$$

where j_{NM} is the current density in the Pd(O) layer. The Q dependence of the rf current in the Pd(O) layer, I_{NM} , and the electric conductivity σ of the Pd(O) films are shown in Figs. 4(c) and 4(d), respectively. In Figs. 4(e) and 4(f), we plot ξ_{DL} and ξ_{FL} with respect to Q and the electric conductivity σ of the Pd(O) layer. Here, the DL and FL torque efficiencies for the $\text{Ni}_{81}\text{Fe}_{19}/\text{Pd}$ film with $Q = 0\%$ are $\xi_{\text{DL}} = 0.0194 \pm 0.0043$ and $\xi_{\text{FL}} = 0.0299 \pm 0.0068$, respectively. These values are consistent with a previous report [41].

Figure 4(e) shows that ξ_{DL} increases while ξ_{FL} decreases with Q for $Q < 0.5\%$. By further increasing Q , both ξ_{DL} and ξ_{FL} decreases with Q . In particular, ξ_{FL} decays rapidly with increasing Q or decreasing σ . In $\text{Ni}_{81}\text{Fe}_{19}/\text{Pd}$ films, the dominant mechanism for the DL-torque generation is the spin Hall effect in the Pd layer but the DL torque originating from the $\text{Ni}_{81}\text{Fe}_{19}/\text{Pd}$ interface is also non-negligible [44,45]. The sizable FL torque for $Q < 1\%$ is consistent with the non-negligible interfacial contribution because the interfacial spin-orbit coupling is the primary source of the FL torque in metallic systems [46]. The clear suppression of the FL torque suggests that the interfacial contribution to the spin-orbit torques decreases with the oxygen incorporation in the Pd layer.

The maximization of ξ_{DL} , shown in Figs. 4(e) and 4(f), can be attributed to a nonmonotonic variation of the spin Hall conductivity σ_{SH} of the Pd layer with respect to the oxygen incorporation. We assume that the DL torque efficiency is expressed as $\xi_{\text{DL}} = T_{\text{int}} \sigma_{\text{SH}}/\sigma$, since the dominant contribution to the DL torque is the bulk spin Hall effect in $\text{Ni}_{81}\text{Fe}_{19}/\text{Pd}$ films [41]. For the bilayer, the spin transparency at the interface, T_{int} , is expressed as [47]

$$T_{\text{int}} = \frac{G^{\uparrow\downarrow} \tanh\left(\frac{d_{\text{NM}}}{2\lambda_{\text{NM}}}\right)}{G^{\uparrow\downarrow} \coth\left(\frac{d_{\text{NM}}}{\lambda_{\text{NM}}}\right) + \frac{G_{\text{NM}}}{2}}, \quad (6)$$

where $G_{\text{NM}} = \sigma/\lambda_{\text{NM}}$, d_{NM} , and λ_{NM} are the spin conductance, the thickness, and the spin relaxation length of the Pd(O) layer, respectively [48]. The spin mixing conductance at the interface $G^{\uparrow\downarrow}$ can be determined by measuring the $\text{Ni}_{81}\text{Fe}_{19}$ -layer thickness t_{FM} dependence of the magnetic damping constant $\alpha = \gamma \hbar g_{\text{eff}}^{\uparrow\downarrow}/(4\pi M_s t_{\text{FM}}^{\text{eff}}) + \alpha_0$, for the $\text{Ni}_{81}\text{Fe}_{19}/\text{Pd}(\text{O})$ films using

$$G^{\uparrow\downarrow} = \frac{\frac{G_{\text{NM}}}{2} \frac{e^2}{h} g_{\text{eff}}^{\uparrow\downarrow}}{\frac{G_{\text{NM}}}{2} - \frac{e^2}{h} g_{\text{eff}}^{\uparrow\downarrow} \coth\left(\frac{d_{\text{NM}}}{\lambda_{\text{NM}}}\right)}, \quad (7)$$

where $g_{\text{eff}}^{\uparrow\downarrow}$ is the effective spin-mixing conductance, α_0 is the intrinsic damping of the $\text{Ni}_{81}\text{Fe}_{19}$ layer, and h is the Planck constant. Assuming that the spin relaxation in the Pd(O) layer is dominated by the Elliott-Yafet mechanism, we estimate the spin diffusion length λ_{NM} for the Pd(O) layers with different Q from the conductivity σ using $\lambda_{\text{NM}}/\sigma = 1.0 \times 10^{-15} \Omega \text{m}^2$ [48]. Using measured values of $g_{\text{eff}}^{\uparrow\downarrow}$ with the estimated λ_{NM} , we determined T_{int} for the films with different Q . Figure 5(a) shows the relation between the electric conductivity σ and the spin Hall conductivity σ_{SH} for the Pd(O) films, obtained under the above assumption. This result shows that σ_{SH} is almost constant for $\sigma > 2 \times 10^4 \Omega^{-1} \text{cm}^{-1}$, whereas σ_{SH} decreases with decreasing σ for $\sigma < 2 \times 10^4 \Omega^{-1} \text{cm}^{-1}$. The distinct difference in the variation of σ_{SH} between the different

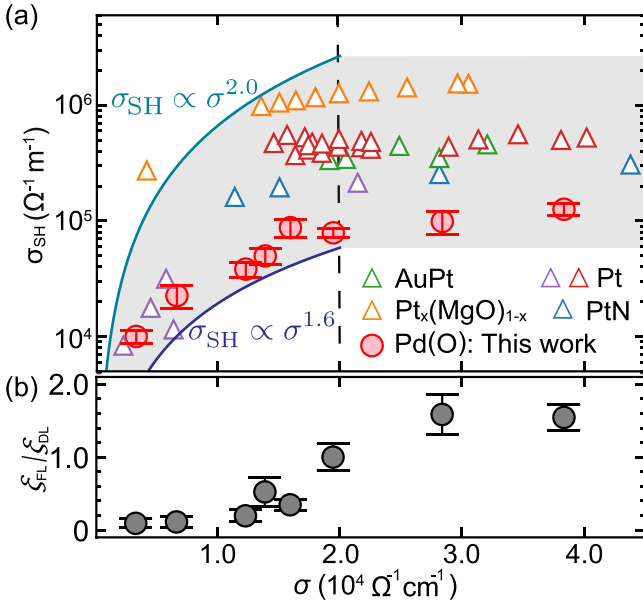


FIG. 5. (a) The relation between the electric conductivity σ and the spin Hall conductivity σ_{SH} for the oxygen-incorporated Pd films (red circles). The dashed line represents $2 \times 10^4 \Omega^{-1} \text{cm}^{-1}$, where the transition of the coherent to the incoherent regime is expected. For comparison, σ_{SH} of Pt and Pt alloys are also plotted (open triangles); PtN films [20]; Pt_xMgO_{1-x} films [19]; AuPt films [43]; Pt films [18,21]. $\sigma_{\text{SH}} \propto \sigma^{1.6}$ and $\sigma_{\text{SH}} \propto \sigma^2$ are suggested by theories of the anomalous and spin Hall effects [16,17]. (b) The dependence of $\xi_{\text{FL}}/\xi_{\text{DL}}$ on σ for the Ni₈₁Fe₁₉/Pd(O) films.

conductivity regimes gives rise to the maximization of ξ_{DL} around $\sigma = 2 \times 10^4 \Omega^{-1} \text{cm}^{-1}$.

The variation of the spin Hall conductivity shown in Fig. 5(a) is consistent with the prediction of the coherent-incoherent crossover of the intrinsic spin Hall effect in the Pd layer. In the conductivity range in Fig. 5(a), the spin Hall effect is dominated by the intrinsic mechanism. In the intrinsic mechanism, the spin Hall conductivity is insensitive to scattering, i.e., impurities and disorder, in the moderately dirty regime where the carrier scattering time is sufficiently long. The reason for this is that, when the carrier scattering time τ is sufficiently long, the intrinsic spin Hall conductivity is governed by the lifetime of the interband excitation, $\tau_b = \hbar/\Delta$, where Δ is the band splitting width [16,25]. The observation that the intrinsic spin Hall conductivity is almost independent of σ for $\sigma > 2 \times 10^4 \Omega^{-1} \text{cm}^{-1}$ is consistent with this scenario. This situation changes when τ is shorter than \hbar/Δ . In this dirty regime, the spin Hall conductivity decreases with decreasing τ , or σ , since the carrier scattering limits the interband excitation that governs the intrinsic spin Hall effect [16]. For transition metals, such as Pd, \hbar/Δ corresponds to around [16] $\sigma = 2 \times 10^4 \Omega^{-1} \text{cm}^{-1}$, suggesting that observed variation of σ_{SH} for the oxygen-incorporated Pd films is consistent with the crossover between the coherent and incoherent regimes of the spin Hall effect. Here, the spin Hall conductivity for $Q = 0\%$ is larger than $\sigma_{\text{SH}} = 3.5 \times 10^4 \Omega^{-1} \text{m}^{-1}$ for Pd obtained from *ab initio* calculations [49]. This suggests that, although the dominant mechanism of the DL torque is the spin Hall effect, a DL torque originating from the inter-

facial spin-orbit coupling cannot be completely neglected in the measured values of ξ_{DL} . The small variation of σ_{SH} for $\sigma > 2 \times 10^4 \Omega^{-1} \text{cm}^{-1}$ in Fig. 5(a) can be attributed to the variation of the interface contribution. Because of the non-negligible interfacial contribution, $g_{\text{eff}}^{\uparrow\downarrow}$ can also be affected by the spin memory loss, suggesting that the estimated T_{int} is the lower bound.

In contrast, the interface contribution can be negligible for $\sigma < 2 \times 10^4 \Omega^{-1} \text{cm}^{-1}$, which is suggested by the negligible $\xi_{\text{FL}}/\xi_{\text{DL}}$, as shown in Fig. 5(b); the bulk spin Hall effect mainly generates the DL torque, while the interfacial spin-orbit coupling mainly generates the FL torque [46], suggesting that the FL torque is much weaker than the DL torque in a system with a negligible interfacial contribution. This supports the idea that the suppression of σ_{SH} for $\sigma < 2 \times 10^4 \Omega^{-1} \text{cm}^{-1}$ is induced by the suppression of the spin Hall conductivity with decreasing σ .

Here, the observed variation of the spin Hall conductivity cannot be attributed to a change of the extrinsic contribution to the spin Hall effect induced by the oxygen incorporation. The reason for this is that the extrinsic contribution can be significant only when the conductivity is higher than around $6 \times 10^4 \Omega^{-1} \text{cm}^{-1}$ because the extrinsic contribution increases with increasing the conductivity, while the intrinsic contribution is insensitive to the conductivity in the coherent regime [18]. The conductivity of the Pd(O) films used in the present study is lower than $4 \times 10^4 \Omega^{-1} \text{cm}^{-1}$, showing that the dominant mechanism of the spin Hall effect is the intrinsic mechanism. The dominant role of the intrinsic spin Hall effect in the Pd(O) layer is supported by the idea that the spin Hall conductivity is insensitive to the conductivity when the conductivity is varied from 2×10^4 to $4 \times 10^4 \Omega^{-1} \text{cm}^{-1}$. Since the intrinsic mechanism dominates the spin Hall effect in the Pd(O) film, a possible suppression of the extrinsic contribution due to the oxygen incorporation can be neglected, compared with the larger intrinsic contribution.

IV. CONCLUSIONS

In summary, we have investigated the spin-orbit torques generated by oxygen-incorporated Pd, Pd(O). We found that the FL torque is strongly suppressed by the oxygen incorporation, which can be attributed to the suppression of the spin-orbit torque originating from the Ni₈₁Fe₁₉/Pd interface. Contrary to the FL torque, the DL torque survives in the Ni₈₁Fe₁₉/Pd(O). We observed that the spin Hall conductivity, determined from the DL torque, is almost unchanged in the devices where the electric conductivity σ is higher than $2 \times 10^4 \Omega^{-1} \text{cm}^{-1}$. By further decreasing the conductivity through the oxygen incorporation, we found that the spin Hall conductivity decreases with decreasing the conductivity. The clear difference in the variation of the spin Hall conductivity can be attributed to the coherent-incoherent crossover of the spin Hall effect. In the Pd(O) films with $\sigma > 2 \times 10^4 \Omega^{-1} \text{cm}^{-1}$, the spin Hall conductivity is governed by the interband excitation. In contrast, in the Pd(O) films with $\sigma < 2 \times 10^4 \Omega^{-1} \text{cm}^{-1}$, the spin Hall conductivity is suppressed by the disorder since the carrier scattering limits the interband excitation that governs the intrinsic spin Hall effect. Although the coherent-incoherent crossover of the spin

Hall effect is predicted to be universal in many transition metals [16], it has been observed only for Pt and Pt-based alloys. The observation of the crossover of the spin Hall effect for Pd supports the generality of this phenomenon, illustrating an important correspondence between the spin Hall effect and the anomalous Hall effect.

For a fundamental understanding of the spin Hall effect, systematic experimental studies on the scaling in various materials are indispensable. In fact, the microscopic understanding of the anomalous Hall effect has been derived from the discovery of the unified experimental scaling of the anomalous Hall conductivity in a diverse set of materials.

Thus, our result provides important information for a better understanding of the spin Hall effect.

ACKNOWLEDGMENTS

This work was supported by Canon Foundation, JSPS KAKENHI (Grant No. 19H00864), JST FOREST Program (Grant No. JPMJFR2032), Asahi Glass Foundation, Academic Development Fund (Keio University Academic Development Funds), and Spintronics Research Network of Japan (Spin-RNJ).

-
- [1] F. Hellman, A. Hoffmann, Y. Tserkovnyak, G. S. D. Beach, E. E. Fullerton, C. Leighton, A. H. MacDonald, D. C. Ralph, D. A. Arena, H. A. Dürr, P. Fischer, J. Grollier, J. P. Heremans, T. Jungwirth, A. V. Kimel, B. Koopmans, I. N. Krivorotov, S. J. May, A. K. Petford-Long, J. M. Rondinelli *et al.*, Interface-induced phenomena in magnetism, *Rev. Mod. Phys.* **89**, 025006 (2017).
- [2] M. I. Dyakonov and V. I. Perel, Current-induced spin orientation of electrons in semiconductors, *Phys. Lett. A* **35**, 459 (1971).
- [3] J. E. Hirsch, Spin Hall Effect, *Phys. Rev. Lett.* **83**, 1834 (1999).
- [4] J. Sinova, D. Culcer, Q. Niu, N. A. Sinitsyn, T. Jungwirth, and A. H. MacDonald, Universal Intrinsic Spin Hall Effect, *Phys. Rev. Lett.* **92**, 126603 (2004).
- [5] S. Murakami, N. Nagaosa, and S. C. Zhang, Dissipationless quantum spin current at room temperature, *Science* **301**, 1348 (2003).
- [6] Y. Kato, R. Myers, A. Gossard, and D. Awschalom, Observation of the spin Hall effect in semiconductors, *Science* **306**, 1910 (2004).
- [7] J. Wunderlich, B. Kaestner, J. Sinova, and T. Jungwirth, Experimental Observation of the Spin-Hall Effect in a Two-Dimensional Spin-Orbit Coupled Semiconductor System, *Phys. Rev. Lett.* **94**, 047204 (2005).
- [8] E. Saitoh, M. Ueda, H. Miyajima, and G. Tatara, Conversion of spin current into charge current at room temperature: Inverse spin-Hall effect, *Appl. Phys. Lett.* **88**, 182509 (2006).
- [9] S. O. Valenzuela and M. Tinkham, Direct electronic measurement of the spin Hall effect, *Nature (London)* **442**, 176 (2006).
- [10] T. Kimura, Y. Otani, T. Sato, S. Takahashi, and S. Maekawa, Room-Temperature Reversible Spin Hall Effect, *Phys. Rev. Lett.* **98**, 156601 (2007).
- [11] J. Sinova, S. O. Valenzuela, J. Wunderlich, C. H. Back, and T. Jungwirth, Spin Hall effects, *Rev. Mod. Phys.* **87**, 1213 (2015).
- [12] R. Karplus and J. M. Luttinger, Hall effect in ferromagnetics, *Phys. Rev.* **95**, 1154 (1954).
- [13] J. Smit, The spontaneous Hall effect in ferromagnetics II, *Physica* **24**, 39 (1958).
- [14] L. Berger, Side-jump mechanism for the Hall effect of ferromagnets, *Phys. Rev. B* **2**, 4559 (1970).
- [15] G. Y. Guo, S. Murakami, T.-W. Chen, and N. Nagaosa, Intrinsic Spin Hall Effect in Platinum: First-Principles Calculations, *Phys. Rev. Lett.* **100**, 096401 (2008).
- [16] T. Tanaka, H. Kontani, M. Naito, T. Naito, D. S. Hirashima, K. Yamada, and J. Inoue, Intrinsic spin Hall effect and orbital Hall effect in $4d$ and $5d$ transition metals, *Phys. Rev. B* **77**, 165117 (2008).
- [17] N. Nagaosa, J. Sinova, S. Onoda, A. H. MacDonald, and N. P. Ong, Anomalous Hall effect, *Rev. Mod. Phys.* **82**, 1539 (2010).
- [18] E. Sagasta, Y. Omori, M. Isasa, M. Gradhand, L. E. Hueso, Y. Niimi, Y. C. Otani, and F. Casanova, Tuning the spin Hall effect of Pt from the moderately dirty to the superclean regime, *Phys. Rev. B* **94**, 060412(R) (2016).
- [19] L. Zhu, L. Zhu, M. Sui, D. C. Ralph, and R. A. Buhrman, Variation of the giant intrinsic spin Hall conductivity of Pt with carrier lifetime, *Sci. Adv.* **5**, eaav8025 (2019).
- [20] N. Soya, H. Hayashi, T. Harumoto, T. Gao, S. Haku, and K. Ando, Crossover of the intrinsic spin Hall effect in the presence of lattice expansion, *Phys. Rev. B* **103**, 174427 (2021).
- [21] S. Dushenko, M. Hokazono, K. Nakamura, Y. Ando, T. Shinjo, and M. Shiraishi, Tunable inverse spin Hall effect in nanometer-thick platinum films by ionic gating, *Nat. Commun.* **9**, 3118 (2018).
- [22] L. Zhu and R. A. Buhrman, Maximizing Spin-Orbit-Torque Efficiency of Pt/Ti Multilayers: Trade-Off between Intrinsic Spin Hall Conductivity and Carrier Lifetime, *Phys. Rev. Appl.* **12**, 051002(R) (2019).
- [23] Y. Tian, L. Ye, and X. Jin, Proper Scaling of the Anomalous Hall Effect, *Phys. Rev. Lett.* **103**, 087206 (2009).
- [24] S. Onoda, N. Sugimoto, and N. Nagaosa, Intrinsic Versus Extrinsic Anomalous Hall Effect in Ferromagnets, *Phys. Rev. Lett.* **97**, 126602 (2006).
- [25] S. Onoda, N. Sugimoto, and N. Nagaosa, Quantum transport theory of anomalous electric, thermoelectric, and thermal Hall effects in ferromagnets, *Phys. Rev. B* **77**, 165103 (2008).
- [26] X. Qiu, K. Narayanapillai, Y. Wu, P. Deorani, D.-H. Yang, W.-S. Noh, J.-H. Park, K.-J. Lee, H.-W. Lee, and H. Yang, Spin-orbit-torque engineering via oxygen manipulation, *Nat. Nanotechnol.* **10**, 333 (2015).
- [27] K.-U. Demasius, T. Phung, W. Zhang, B. P. Hughes, S.-H. Yang, A. Kellock, W. Han, A. Pushp, and S. S. Parkin, Enhanced spin-orbit torques by oxygen incorporation in tungsten films, *Nat. Commun.* **7**, 10644 (2016).
- [28] H. An, Y. Kageyama, Y. Kanno, N. Enishi, and K. Ando, Spin-torque generator engineered by natural oxidation of Cu, *Nat. Commun.* **7**, 13069 (2016).

- [29] H. An, T. Ohno, Y. Kanno, Y. Kageyama, Y. Monnai, H. Maki, J. Shi, and K. Ando, Current-induced magnetization switching using an electrically insulating spin-torque generator, *Sci. Adv.* **4**, eaar2250 (2018).
- [30] T. Gao, A. Qaiumzadeh, H. An, A. Musha, Y. Kageyama, J. Shi, and K. Ando, Intrinsic Spin-Orbit Torque Arising from the Berry Curvature in a Metallic-Magnet/Cu-Oxide Interface, *Phys. Rev. Lett.* **121**, 017202 (2018).
- [31] R. Bansal, G. Nirala, A. Kumar, S. Chaudhary, and P. K. Muduli, Large spin Hall angle in β -W thin films grown on CoFeB without oxygen plasma, *SPIN* **08**, 1850018 (2018).
- [32] Y. Kageyama, Y. Tazaki, H. An, T. Harumoto, T. Gao, J. Shi, and K. Ando, Spin-orbit torque manipulated by fine-tuning of oxygen-induced orbital hybridization, *Sci. Adv.* **5**, eaax4278 (2019).
- [33] M. Brun, A. Berthet, and J. C. Bertolini, XPS, AES and Auger parameter of Pd and PdO, *J. Electron Spectrosc. Relat. Phenom.* **104**, 55 (1999).
- [34] G. K. Reddy, C. Ling, T. C. Peck, and H. Jia, Understanding the chemical state of palladium during the direct NO decomposition—influence of pretreatment environment and reaction temperature, *RSC Adv.* **7**, 19645 (2017).
- [35] A. Baylet, P. Marécot, D. Duprez, P. Castellazzi, G. Groppi, and P. Forzatti, *In situ* Raman and *in situ* XRD analysis of PdO reduction and Pd oxidation supported on γ -Al₂O₃ catalyst under different atmospheres, *Phys. Chem. Chem. Phys.* **13**, 4607 (2011).
- [36] H. P. Klug and L. E. Alexander, X-ray diffraction procedures for polycrystalline and amorphous materials, in *X-Ray Spectrometry* (John Wiley & Sons, New York, 1974), Vol. 4, p. 960.
- [37] L. Liu, T. Moriyama, D. C. Ralph, and R. A. Buhrman, Spin-Torque Ferromagnetic Resonance Induced by the Spin Hall Effect, *Phys. Rev. Lett.* **106**, 036601 (2011).
- [38] A. Okada, Y. Takeuchi, K. Furuya, C. Zhang, H. Sato, S. Fukami, and H. Ohno, Spin-Pumping-Free Determination of Spin-Orbit Torque Efficiency from Spin-Torque Ferromagnetic Resonance, *Phys. Rev. Appl.* **12**, 014040 (2019).
- [39] S. Karimeddiny, J. A. Mittelstaedt, R. A. Buhrman, and D. C. Ralph, Transverse and Longitudinal Spin-Torque Ferromagnetic Resonance for Improved Measurement of Spin-Orbit Torque, *Phys. Rev. Appl.* **14**, 024024 (2020).
- [40] C.-F. Pai, Y. Ou, L. H. Vilela-Leão, D. C. Ralph, and R. A. Buhrman, Dependence of the efficiency of spin Hall torque on the transparency of Pt/ferromagnetic layer interfaces, *Phys. Rev. B* **92**, 064426 (2015).
- [41] A. Ghosh, K. Garello, C. O. Avci, M. Gabureac, and P. Gambardella, Interface-Enhanced Spin-Orbit Torques and Current-Induced Magnetization Switching of Pd/Co/Alox Layers, *Phys. Rev. Appl.* **7**, 014004 (2017).
- [42] V. Tshitoyan, C. Ciccarelli, A. P. Mihai, M. Ali, A. C. Irvine, T. A. Moore, T. Jungwirth, and A. J. Ferguson, Electrical manipulation of ferromagnetic NiFe by antiferromagnetic IrMn, *Phys. Rev. B* **92**, 214406 (2015).
- [43] M. Obstbaum, M. Decker, A. K. Greitner, M. Haertinger, T. N. G. Meier, M. Kronseder, K. Chadova, S. Wimmer, D. Ködderitzsch, H. Ebert, and C. H. Back, Tuning Spin Hall Angles by Alloying, *Phys. Rev. Lett.* **117**, 167204 (2016).
- [44] K. Kondou, H. Sukegawa, S. Mitani, K. Tsukagoshi, and S. Kasai, Evaluation of spin Hall angle and spin diffusion length by using spin current-induced ferromagnetic resonance, *Appl. Phys. Express* **5**, 073002 (2012).
- [45] Z. Tang, Y. Kitamura, E. Shikoh, Y. Ando, T. Shinjo, and M. Shiraishi, Temperature dependence of spin Hall angle of palladium, *Appl. Phys. Express* **6**, 083001 (2013).
- [46] V. P. Amin and M. D. Stiles, Spin transport at interfaces with spin-orbit coupling: Phenomenology, *Phys. Rev. B* **94**, 104420 (2016).
- [47] W. Zhang, W. Han, X. Jiang, S.-H. Yang, and S. S. P. Parkin, Role of transparency of platinum-ferromagnet interfaces in determining the intrinsic magnitude of the spin Hall effect, *Nat. Phys.* **11**, 496 (2015).
- [48] Y. Liu, Z. Yuan, R. J. H. Wesselink, A. A. Starikov, M. van Schilfhaarde, and P. J. Kelly, Direct method for calculating temperature-dependent transport properties, *Phys. Rev. B* **91**, 220405(R) (2015).
- [49] G. Y. Guo, *Ab initio* calculation of intrinsic spin Hall conductivity of Pd and Au, *J. Appl. Phys.* **105**, 07C701 (2009).